Internal decoherence in nano-object interferometry due to phonons

C. Henkel[1] and R. Folman[2]

[1]*Universität Potsdam, Institut für Physik und Astronomie, 14476 Potsdam, Germany*

[2]*Ben-Gurion University of the Negev, Department of Physics, Beer Sheva 84105, Israel*[a]

(*Electronic mail: henkel@uni-potsdam.de)

(Dated: 27 April 2022)

We discuss the coherent splitting and recombining of a nanoparticle in a mesoscopic "closed-loop" Stern-Gerlach interferometer in which the observable is the spin of a single impurity embedded in the particle. This spin, when interacting with a pulsed magnetic gradient, generates the force on the particle. We calculate the internal decoherence which arises as the displaced impurity excites internal degrees of freedom (phonons) that may provide *Welcher Weg* information and preclude interference. We estimate the constraints this decoherence channel puts on future interference experiments with massive objects. We find that for a wide range of masses, forces and temperatures, phonons do not inhibit Stern-Gerlach interferometry with micro-scale objects. However, phonons do constitute a fundamental limit on the splitting of larger macroscopic objects if the applied force induces phonons.

I. INTRODUCTION

Quantum Mechanics (QM) and General Relativity (GR), the latter being the current theory of gravity, are the two pillars of modern physics. The quantum nature of gravity, or the unification of these two pillars, has been an open question of utmost importance for decades now. While theory has not been able to find a satisfactory solution to this question, it is of paramount importance for experiments to deliver hints. We discuss here a nano-object interferometer aimed at delivering such hints as they emerge from the interface between QM and GR. Such an interferometer may probe gravity-related ideas, from the mainstream quantum of gravitation[1], named the graviton, to speculative ideas, such as those of Penrose concerning gravitationally induced collapse (see, e.g., Ref. [2]) or the short-range correction to gravity, the so-called fifth force. For an in-depth overview, see for example Refs. [3–9].

Another specific motivation for such an interferometer relates to the foundations of QM. It will push the limits to which the accuracy of QM is tested, by several orders of magnitude: both in the amount of mass that is being put in a spatial superposition, and in the size of the spatial splitting. Another contribution to the foundations of QM would be the ability to test continuous spontaneous localization models. These are of crucial importance in the search for extensions to QM. For a more complete review of underlying concepts, see for example Refs. [10] and [11].

Finally, a third motivation is quantum technology. In addition to the quantum computer, there is metrology. A nano-object interference experiment will bring about cutting-edge metrological capabilities, e.g., in the measurement of gravity[12], including geodesic studies and mineral searches, or in acceleration sensing.

Let us briefly note that the aims of such an endeavor are difficult to be obtained by laser-based matter interferometry. First, laser pulses can be absorbed and scattered by the nano-object (nOb) and, as already shown in experiments, they heat up the object and can lead to its opaqueness or destruction.[13] Light scattering also increases the spatial decoherence rate, if it can resolve the two paths. Second, laser-based matter-wave interferometry requires an appropriate optical transition, and this severely restricts its applicability to massive solid objects. Such optical transitions have been suggested[14], but they suffer from two major drawbacks: (a) they typically require cryogenic temperatures and as noted the light impinging on the object heats it and cooling a free-space object is extremely hard; (b) they give very low recoil velocities and thousands of these transitions would be required for significant splitting in a short time. For example, for a 10^{-20} kg nOb, the optical recoil velocity is on the order of 10^{-8} m/s whereas a continued acceleration of say $100 \, \text{m/s}^2$ for a short period of say $100 \, \mu\text{s}$ gives a velocity six orders of magnitude higher. Here we consider a Stern-Gerlach interferometer (SGI) which utilizes magnetic gradients rather than light pulses to generate the spatial superposition.

The state of the art for nOb interferometry utilises a beam of heavy molecules impinging on a grating. The heaviest molecules put in a superposition to date consist of up to 2000 atoms.[15,16] The SGI may go far beyond this limit. In the spirit of molecular-beam experiments, several proposals exist for slit-type experiments with higher masses, specifically including solid nObs.[10,17,18] In these proposed experiments, none of which has been realized yet, the signal is a spatial interference pattern, reminiscent of the double-slit interference pattern. These proposals face several challenges. For example, for spatial interference patterns to form, a long time-of-flight (TOF) is required, and as the decoherence rate of delocalized massive-object states is expected to be high, a prolonged TOF seems impractical. Furthermore, for many of these configurations, the periodicity of the interference pattern is expected to be extremely small, so that high spatial resolution is required for detection, a resolution which may be beyond available technology, especially for high-efficiency detection.

The SGI considered here is a completely different route for realizing such an interferometer, as shown in Fig. 1. A single spin embedded in the nano-object is first put in a superposi-

---

[a]Also at Ilse Katz Institute for Nanoscale Science and Technology, Beer Sheva, Israel

tion of opposite spins. When moving through a magnetic-field gradient, the two spin orientations experience opposite forces, and this splits the wavefunction of the entire nOb into two wave-packets (WPs), effectively generating spin-momentum entanglement. Reversing the opposite forces is then used to bring the two WPs back together again. Such an interferometer has three crucial advantages: (a) the splitting is active, namely, a real force is utilized, and it does not depend on expanding the WP; consequently, large splitting distances may be achieved in a short time; (b) the signal forms independently of any TOF and, as the recombination is also active, it may be done in a short time; (c) the observable is spin population, as in modern atom interferometry; in contrast to spatial fringes, its detection does not require high spatial resolution.
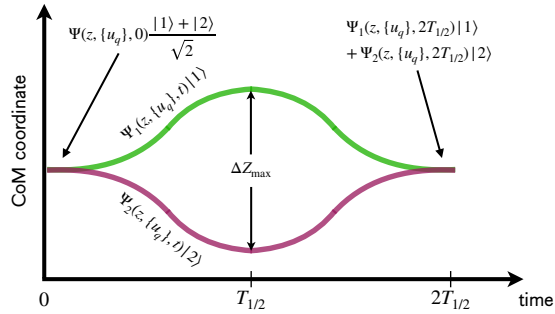

FIG. 1. Sketch of the Stern-Gerlach interferometer (SGI), adapted from Fig. 1 in Ref. 19. Along the two paths, the wavepackets behave distinctly different with respect to the center-of-mass coordinate (CoM) z and the amplitudes $\{u_q\}$ of the internal phonon modes. The maximum splitting ΔZ_{max} is reached at $T_{1/2}$ which is half the time required to close the loop.
Adapted with permission from Y. Margalit, O. Dobkowski, Z. Zhou, O. Amit, Y. Japha, S. Moukouri, D. Rohrlich, A. Mazumdar, S. Bose, C. Henkel, and R. Folman, "Realization of a complete Stern-Gerlach interferometer: Towards a test of quantum gravity," *Science Adv.* **7**, eabg2879 (2021). Copyright (2021) The Authors under licence CC BY 4.0, DOI:10.1126/sciadv.abg2879.

We recently demonstrated the coherence of a Stern-Gerlach "closed-loop" interferometer with ultracold atoms and discussed the possibility of realizing such an interferometer with a nano-particle.[19] Decoherence, or lack of coherence, comes from two very different physical processes, the first originating in the coupling of the nOb to the environment, and the second originating in the fact that the loop is not completely closed, coined the "Humpty-Dumpty" effect (see Ref. 19 and references therein). The latter type of decoherence, independent of the environment, depends on the final overlap of several wave functions, that of the external degrees of freedom (position, momentum and rotation, for the latter, see for example Ref. 20 and references therein), as well as internal degrees of freedom, including spin and phonons, the latter being the topic of this work. If the wave functions of the WPs along the two paths become orthogonal, no interference is possible. Orthogonality may arise from the non-identical phonon excitations due to the applied Stern-Gerlach force along the two paths the WPs take. As we show in the following, this is dependent on the nOb size and temperature and on the applied

force (i.e., the magnetic gradient).

As we would like to focus solely on decoherence due to phonons, in the following we assume that all other types of decoherence are negligible. However, let us briefly note the different types of decoherence which should be considered, and the works which have already addressed them. To begin with, spin coherence is crucial if spin is the observable of the interferometer. The T_1 and T_2 times of the spin must be longer than the interferometer time. For the nitrogen-vacancy center embedded in a nano-diamond as discussed in this work, a room-temperature coherence time of a few hundred μs was observed.[21] Blackbody radiation (BBR) is a source of spatial decoherence.[10,22–25] Collisions with background gas are also an important source of decoherence.[14,24] Any charging of the nOb would again cause decoherence through the electrostatic coupling to the environment.[26] See also Ref. 19 and references therein.

Many works have already considered the importance of internal temperatures for lower decoherence in such nOb interferometers. Specifically, concerning BBR, it has been suggested that internal state cooling of the neutral test masses in addition to external cooling in opto-mechanical cavities would prove to be greatly beneficial.[27] Furthermore, quite a few works dealt with the quantum dynamics of nOb phonons.[28–30] However, as far as we know, this is the first treatment of phonons as a source of decoherence.

II. MODEL

A. Hamiltonian

We envision a nano-object embedded with a single spin, such as a nano-diamond with a single nitrogen-vacancy center. The model for the nano-object is based on microscopic models of magnetic materials, see, e.g., Ref. 31. The atoms of the object are characterized by their positions $\mathbf{r}_i$ and momenta $\mathbf{p}_i$. For our purposes, only a single atom, say at site number s, carries a spin $\mathbf{S}$. For definiteness we assume $S = \frac{1}{2}$. The Hamiltonian is a sum of mechanical and magnetic terms $H = H_1 + H_2(t)$ with

$$H_1 = \sum_i \frac{\mathbf{p}_i^2}{2m} + \sum_{\langle i,j \rangle} V(\mathbf{r}_i - \mathbf{r}_j) \tag{1}$$

$$H_2(t) = -\mu \mathbf{S} \cdot \mathbf{B}(\mathbf{r}_s, t) \tag{2}$$

where m is the single-atom mass (assumed identical for simplicity) and μ the magnetic moment (the spin $\mathbf{S}$ is taken dimensionless). We do not take into account collective magnetic interactions, such as the diamagnetic interaction[32,33], as they are not expected to excite phonons.

The second sum in Eq. (1) can be restricted to nearest neighbor sites i, j and involves the bond potential

$$V(\mathbf{r}_i - \mathbf{r}_j) = \frac{K}{2}(\mathbf{r}_i - \mathbf{r}_j)^2 + \text{anharmonic terms} \tag{3}$$

with a common spring constant K. From this model, we get

TABLE I. Typical orders of magnitude for nano-particles made from diamond.

magnetic gradient[a]	$10^6\,\text{T/m}$
particle mass	$10^6 - 10^{10}\,\text{amu}$
size (diameter)[b]	$L = 10 - 200\,\text{nm}$
magnetic moment μ	$1\,\mu_B = h \times 14\,\text{GHz/T}$
acceleration	$6000 - 0.6\,\text{m/s}^2$
lowest phonon mode[c]	
$\omega_1/2\pi = c/2L$	$900 - 45\,\text{GHz}$
de Broglie wavelength[d] λ_{cm}	$T_{cm} = 293\,\text{K}: \quad 10^{-14} - 10^{-16}\,\text{m}$
phonon coherence length[e] λ_{ph}	$T_{ph} = 4\,\text{K}: \quad 10^{-13} - 10^{-15}\,\text{m}$

[a] Achievable with atom chips $1\,\mu\text{m}$ away from a $1 \times 1\,\mu\text{m}^2$ wire with $10^9\,\text{A/cm}^2$ current density.
[b] Unit cell with $a = 3.6\,\text{Å}$ and 8 C atoms.
[c] Speed of sound $c = 17.5\,\text{km/s}$.
[d] Estimated as $\lambda_{cm} = \hbar(Mk_B T_{cm})^{-1/2}$ with the center-of-mass temperature T_{cm}.
[e] Estimated as $\lambda_{ph} = \hbar(Mk_B T_{ph})^{-1/2}$ with the internal (phonon) temperature T_{ph}.

for the center-of-mass coordinate $\mathbf{R} = (1/N)\sum_i \mathbf{r}_i$ and its corresponding momentum $\mathbf{P} = \sum_i \mathbf{p}_i$ the equation of motion

$$\dot{\mathbf{P}} = -\sum_i \frac{\partial H}{\partial \mathbf{r}_i} = \mu \sum_\alpha S_\alpha \frac{\partial B_\alpha}{\partial \mathbf{r}_s} \qquad (4)$$

where the interaction potential Eq. (3) drops out by Newton's *actio = reactio*. Typical accelerations are given in Table I.

We start for the phonons with a simple one-dimensional model with N atoms in a linear chain having a total mass of $mN = M$. If we interpret the coordinates z_i as the deviation from equilibrium positions spaced by the equilibrium bond length (lattice constant) a, we get a chain model whose phonon spectrum in the harmonic approximation is given by (force-free or Neumann boundary conditions)

$$\omega(q) = \sqrt{\frac{4K}{m}} \sin\frac{qa}{2}, \qquad q = \frac{\pi}{L}\{0, 1, 2, \ldots, N_x - 1\} \quad (5)$$

where $L = aN$ is the total length of the chain. The mode amplitudes u_q (illustrated in Fig. 2) can be computed from the projection

$$u_q = \frac{2}{N}\sum_n z_n \cos[(n + \tfrac{1}{2})qa], \quad q \neq 0 \qquad (6)$$

and for them, we get the equations of motion

$$\frac{d^2 u_q}{dt^2} = -\omega^2(q)u_q + \frac{2\mu}{M}\cos[(s + \tfrac{1}{2})qa]\sum_\alpha S_\alpha \frac{\partial B_\alpha}{\partial z_s} \qquad (7)$$

where the integer s labels the equilibrium position of the impurity spin (the left end of the chain is at $s = 0$).[34] Finally, the spin itself precesses according to the Larmor equation

$$\frac{d\mathbf{S}}{dt} = \frac{\mu}{\hbar}\mathbf{S} \times \mathbf{B}(\mathbf{r}_s, t) \qquad (8)$$

We consider here the simplest setting where the magnetic field is aligned to the z-axis and is a linear function $B_z(z, t) =$
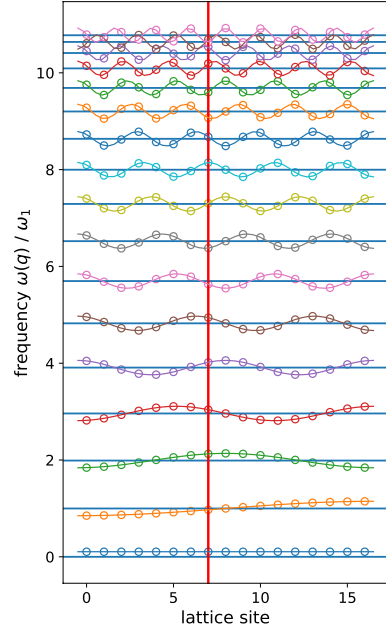

FIG. 2. Sketch of phonon modes (standing waves) for a linear chain. The total length is covered by an integer multiple of half the wavelength. The vertical red line marks the position of the impurity spin. Frequencies scaled to the fundamental tone $\omega_1 = \pi c/L$ with the speed of sound c and length $L = 17$ unit cells. The phonon amplitude is represented by the displacements of the circles, but note that in this linear model, this is actually a longitudinal phonon. The zero-frequency mode corresponds to a displacement of the chain as a whole (center of mass mode).

$B_0 + b(t)z$. Indeed, this is the experimental configuration used by the atomic SGIs[19]. The linear field significantly simplifies the dynamics, as there is no coupling of the CoM, spin and phonon degrees of freedom. This is valid provided the ratio $|b(t)\mathbf{R}/B_0|$ remains small enough to neglect the contributions from transverse components of the magnetic field (required by $\text{div}\,\mathbf{B} = 0$).

In the "spin up" or "down" configurations, the spin vector $\mathbf{S}(t) = \pm\frac{1}{2}\mathbf{e}_z$ will thus be stationary (no precession, no spin flips). The Stern-Gerlach force becomes independent of the nano-object position, and we may solve Eqs. (4, 7) easily:

$$P(t) = P(0) \pm \frac{\mu}{2}\int_0^t dt'\, b(t') \qquad (9)$$

$$Z(t) = Z(0) + \frac{1}{M}\int_0^t dt'\, P(t') \qquad (10)$$

$$u_q(t) = u_q(0)\cos\omega_q t + \frac{\dot{u}_q(0)}{\omega_q}\sin\omega_q t \qquad (11)$$

$$\pm \frac{\mu}{M\omega_q}\cos[(s + \tfrac{1}{2})qa]\int_0^t dt'\, b(t')\sin[\omega_q(t - t')]$$

The $\pm$ sign of the spin projection thus determines the direction of the momentum, as well as the sign of the phonon amplitude. The equations of motion being linear, these expressions are equally valid, whether the variables are treated classically or as quantum operators (Heisenberg picture).

III. OVERLAP AND CONTRAST

The solution presented in Eqs. (9–11) determines the contrast of the spin interference signal in the following way. The key element is the overlap between the wavepackets for the center-of-mass degree of freedom (DoF) and the phonon DoFs that have evolved with either sign $\pm$ of the spin projection.

A. Center of mass

To illustrate our method of calculation, we first calculate the overlap for the center of mass (CoM). As noted in the introduction, we will eventually assume that it is perfect, so that loss of contrast is only due to orthogonality between phonon excitations.

Consider for the CoM state an initial pure state $|\psi\rangle$, and rewrite the solution for momentum $P(t)$ and position $Z(t)$ as the action of some displacement operator $D_\pm$ where the spin sign $\pm$ corresponds to opposite displacement directions:

$$\text{spin up:} \qquad P(t) = D_+^\dagger P(0) D_+$$
$$Z(t) = D_+^\dagger [Z(0) + P(0)t/M] D_+$$
$$\text{spin down:} \qquad P(t) = D_-^\dagger P(0) D_-$$
$$Z(t) = D_-^\dagger [Z(0) + P(0)t/M] D_- \qquad (12)$$

The overlap in question can then be written as

$$\text{Tr}\left(D_+ |\psi\rangle\langle\psi| D_-^\dagger\right) = \langle\psi| D_-^\dagger D_+ |\psi\rangle \qquad (13)$$

This goes down to zero contrast in a Gaussian fashion when the splitting exceeds the width of the initial state $|\psi\rangle$, as expected for orthogonal states.

Since the inverse displacement $D_-^\dagger$ is the same as D_+, the displacement operators can be combined into one operator D that depends on the relative splittings $\Delta Z(t)$, $\Delta P(t)$ between the spin-down and spin-up trajectories. From this viewpoint, the overlap may be understood as the amplitude to stay in the initial state $|\psi\rangle$ after applying the operator D. Such an amplitude is known in scattering as the Debye-Waller factor (see, e.g., Ref. 35 and 36), and may also be related to the zero-phonon line in molecular spectroscopy[37,38].

It is now a well-known identity (sometimes called the Bloch formula) that the expectation value of D is related to the Wigner representation $W(z, p)$ of the wave function $|\psi\rangle$, notably its double Fourier transform[39–42]

$$\langle\psi| D |\psi\rangle = \chi(k, s) = \int dx\, dp\, W(z, p)\, e^{i(kz - sp)}. \qquad (14)$$

The latter is also known as characteristic function for symmetrically ordered products. Its arguments correspond to the displacements in phase space: $k = \Delta P(t)/\hbar$, $s = \Delta Z(t)/\hbar$ that can be read off from Eq. (9).

The value $\chi(0,0) = 1$ corresponds to full contrast when the displacements in position and momentum are exactly zero. This defines the target conditions for a "closed loop" in phase space. Any deviations from them therefore characterize the

accuracy that is needed to close the interferometer. In interferometry, it is well known that a non-closed loop generates a so-called separation phase proportional to $\Delta P(t)$ and $\Delta Z(t)$.[43,44] The expression (14) corresponds to the average of the corresponding phase factor over the initial position and momentum distribution.

The initial distribution is indeed likely to be nonpure, and the advantage of using the Wigner characteristic function is that it can be carried simply through, if in Eqs. (13, 14) we are dealing with a density operator ρ rather than the pure state $|\psi\rangle$. If we assume for simplicity that the initial Wigner function is a Gaussian with variances $\sigma_p^2 = M k_B T_{cm}$ (kinetic temperature T_{cm} for the center-of-mass DoF) and σ_z^2, we get the contrast reduction factor

$$C_{cm} = |\text{tr}(D\rho)| = |\chi(\Delta P(t)/\hbar, \Delta Z(t)/\hbar)|$$
$$= \exp\left[-\tfrac{1}{2}\Delta P(t)^2 \sigma_z^2/\hbar^2 - \tfrac{1}{2}\Delta Z(t)^2 \sigma_p^2/\hbar^2\right] \qquad (15)$$

The characteristic (rms) width of this Gaussian in $\Delta Z(t)$ is given by the spatial coherence length $\hbar/\sigma_p = \lambda_{cm}$ that coincides simply with the thermal de Broglie wavelength λ_{cm} of the nOb (see Table I). This suggests formidable precision requirements for closing the phase-space loop. It turns out, however, that one may confine the nOb in some potential and cool its CoM motion down to the ground state, thereby increasing its coherence length.[45–48]

B. Internal degrees of freedom (phonons)

The decoherence due to phonons can be estimated in a similar way. Consider first a fixed phonon mode with frequency $\omega_q \neq 0$. Along the two interferometer arms, the amplitude u_q of this mode suffers a differential displacement in phase space given by, from Eq. (11):

$$\Delta u_q(t) = \frac{2\mu}{M\omega_q} \cos[(s+\tfrac{1}{2})qa] \int_0^t dt'\, b(t') \sin[\omega_q(t-t')]$$
$$\Delta \dot{u}_q(t) = \frac{2\mu}{M} \cos[(s+\tfrac{1}{2})qa] \int_0^t dt'\, b(t') \cos[\omega_q(t-t')] \quad (16)$$

Now consider this mode to be initially in thermal equilibrium at the (internal) temperature T_{ph}. Its contribution to the energy in Eq. (1) is $E_q = \tfrac{1}{4}M(\dot{u}_q^2 + \omega_q^2 u_q^2)$, the magnetic interaction energy being an irrelevant constant in a slowly varying field. The initial phonon mode amplitude thus has a Gaussian Wigner function with variances $\sigma_{u,q}^2 = 2k_B T_{ph}/(M\omega_q^2)$ in displacement and $\sigma_{\dot{u},q}^2 = 2k_B T/M$ in the corresponding velocity. These variances actually provide the classical limit only: at low temperatures, the replacement

$$k_B T_{ph} \mapsto \tfrac{1}{2}\hbar\omega_q \coth\frac{\beta\omega_q}{2}, \qquad \beta = \frac{\hbar}{k_B T_{ph}} \qquad (17)$$

applies to get the correct Wigner function.[49] The width in amplitude $\sigma_{u,q}$ at zero temperature for the lowest phonon mode is, at realistic temperatures, comparable to the thermal phonon coherence length λ_{ph} given in Table I.

This Wigner function is invariant under the rotation in phase space (first line of Eq. (11)), this is why we may focus on the displacements (16). For the contrast reduction due to phonon mode q, we need the variables k_q, s_q in the displacement operator $D_q = \exp[\mathrm{i}(k_q u_q - s_q \dot{u}_q)]$. The amplitude operators u_q and $\dot{u}_q$ satisfy the commutation relations

$$[u_q, \dot{u}_{q'}] = \frac{2\mathrm{i}\hbar}{M}\delta_{qq'} \qquad (18)$$

that follow from Eq. (6), and we find $k_q = M\Delta\dot{u}_q(t)/2\hbar$, $s_q = M\Delta u_q(t)/2\hbar$. The overlap for the mode q thus generates a contrast

$$C_q = \exp\left[-\tfrac{1}{2}k_q^2\sigma_{u,q}^2 + \tfrac{1}{2}s_q^2\sigma_{\dot{u},q}^2\right]$$
$$= \exp\left[-\frac{M\omega_q}{8\hbar}\left(\Delta u_q(t)^2 + \frac{\Delta\dot{u}_q(t)^2}{\omega_q^2}\right)\coth\frac{\beta\omega_q}{2}\right] \qquad (19)$$

We can here read off the characteristic phonon coherence "length" relative to which the splitting $\Delta u_q(t)$ of the phonon amplitude between the two interferometer arms must be nullified. For low-frequency modes (i.e., $\hbar\omega_q \ll k_B T_{\mathrm{ph}}$), this scale is simply given by the thermal de Broglie wavelength with $\lambda_{\mathrm{ph}} = \hbar/(Mk_B T_{\mathrm{ph}})^{1/2}$ (in the pm range or below, see Table I). The splitting in the phase space of phonon amplitude and momentum can be visualized as in Fig. 3. (A similar picture would represent the results obtained in Sec. III A for the CoM mode.) We also recall the alternative interpretation in terms of a Debye-Waller factor: the contrast depends on the probability that the excitation of the mode u_q in one path of the WP relative to the other does *not* differ by a single phonon quantum.
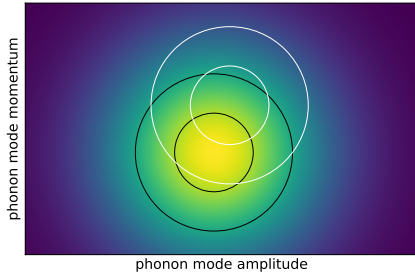

FIG. 3. Splitting in the phase space of a fixed phonon mode. The contrast in the interferometer is determined by the overlap between the distributions illustrated by black contours (with color shading) and white contours.

The two terms in the parenthesis of Eq. (19) can be combined into a complex, finite-window Fourier transform. Introducing the time-dependent acceleration $a(t) = \frac{\mu}{M}b(t)$ and the integral (with dimension velocity)

$$a(\omega_q, t) = \int_0^t \mathrm{d}t'\, a(t')\, \mathrm{e}^{\mathrm{i}\omega_q(t'-t)} \qquad (20)$$

we can write

$$\Delta u_q(t)^2 + \frac{\Delta\dot{u}_q(t)^2}{\omega_q^2} = \frac{4}{\omega_q^2}\cos^2[(s+\tfrac{1}{2})qa]|a(\omega_q, t)|^2 \qquad (21)$$

The extension to the full phonon spectrum is immediate if we assume that the variables $\{u_q, \dot{u}_q\}$ for q in the Brillouin zone describe the normal modes of the chain of atoms. In the harmonic approximation, this is obviously true, and the initial state thus factorizes into a product of thermal states per normal mode. The overlaps per mode multiply, and we get the phonon-based contrast reduction in the form

$$C_{\mathrm{ph}} = \exp\left[-\sum_q \frac{M}{2\hbar\omega_q}\coth\left(\tfrac{1}{2}\beta\omega_q\right)\cos^2[(s+\tfrac{1}{2})qa]|a(\omega_q, t)|^2\right] \qquad (22)$$

A similar technique has been used for the dephasing of a qubit whose energy splitting couples to a phonon bath.[50,51]

In the following section, we discuss the sum over all modes in Eq. (22). To get a qualitative picture, consider first the behaviour of the terms in the sum as a function of phonon frequency ω_q. A sketch is provided in Fig. 4. The main feature is the Fourier spectrum $a(\omega_q, t = 2T_{1/2})$ of the acceleration that is nonzero in a range of frequencies $0 < \omega \lesssim 2\pi/T_{1/2}$. Here, the half duration $T_{1/2}$ of the interferometer loop corresponds to the moment of maximum wavepacket splitting. The vertical lines with symbols illustrate the positions of the phonon eigenfrequencies, they are approximately harmonics of the 'fundamental tone' $\omega_1/2\pi = c/2L$ where c is the speed of sound. The curves provide an upper limit to the summands in Eq. (22), the symbols give smaller values because they take into account the phonon mode amplitude $\cos[(s+\tfrac{1}{2})qa]$. Impurity spins located near the nOb center present two advantages: their overlap with the fundamental mode is small there (see Fig. 2), and their spin coherence time is maximal because they avoid enhanced surface noise.[52] Spins of nitrogen-vacancy (NV) centers in nanodiamonds have already exhibited a room-temperature coherence time of $200\,\mu\mathrm{s}$.[21] While it may be assumed that significant material engineering will improve these numbers[53] (the state of the art for room-temperature bulk is $3\,\mathrm{ms}$[54]), even $200\,\mu\mathrm{s}$ is enough for a chip-based Stern-Gerlach interferometer to achieve significant splitting. Utilising well-known NV techniques (e.g., recent work of the Ben-Gurion University of the Negev group[55–57]), we do not see any fundamental spin-related obstacles.

C. Discrete phonon spectrum (small objects)

The object is small if its fundamental tone is much higher than the inverse duration of the splitting pulse, i.e., $\omega_1 T_{1/2} \gg 2\pi$. With $T_{1/2} = 30\,\mu\mathrm{s}$ and $c \approx 20\,\mathrm{km/s}$ (diamond), this applies for objects with $L < 30\,\mathrm{cm}$, i.e. for any realistic small particle. The amount of orthogonality 'hidden' in the phonon amplitudes along the spin up and down paths of the wavepacket is then determined by the tails of the Fourier spectrum $a(\omega, 2T_{1/2})$ of the nOb acceleration (see Fig. 4). We consider for definiteness three simple protocols for the pulsed magnetic gradient. They have in common a zero net velocity shift (in order to close the loop for the center-of-mass DoF) and their duration $2T_{1/2}$. Moving for simplicity the moment
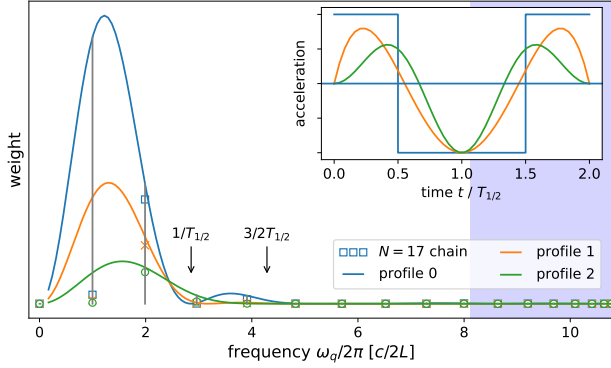
FIG. 4. Sketch of the contribution of individual phonon modes to the interference contrast C_{ph}. We plot the terms under the sum in Eq. (22) as a function of phonon frequency, scaled to the fundamental tone $\omega_1/2\pi = c/(2L)$. The solid lines give an upper limit, discrete phonons are marked by vertical lines, the symbols below the upper limit ($\square$, $\times$, $\circ$) include the squared amplitude of the phonon standing wave at the spin site $s = 7 \simeq N/2$. In the indigo shading, $\hbar\omega_q \geq k_B T_{ph}$ with the phonon temperature T_{ph}. Profiles 0, 1, 2: acceleration protocols $a_0(t)$, $a_1(t)$, $a_2(t)$ of Eqs. (23–25), the last one (green) having the smoothest switching-on and being the most adiabatic, see inset. The width of the spectrum is inversely proportional to the duration $T_{1/2}$ of the closed loop (arrows). Parameters: chain with $N = 17$ atoms, duration of applied forces compared to sound roundtrip $2T_{1/2} = 1.4L/c$, (internal) temperature $k_B T_{ph} = 8.1\hbar\omega_1$.

of maximum splitting to $t = 0$, we take for $-T_{1/2} \leq t \leq T_{1/2}$:

$$a_0(t) = \pm a_{max} \qquad \text{(square profile, see inset Fig. 4)} \quad (23)$$

$$a_1(t) = a_{max}[-1 + 6(t/T_{1/2})^2 - 5(t/T_{1/2})^4] \quad (24)$$

$$a_2(t) = -\frac{a_{max}}{2}[\cos(\pi t/T_{1/2}) + \cos(2\pi t/T_{1/2})] \quad (25)$$

Their Fourier transforms have envelopes that scale with $1/\omega^{n+1}$ ($n = 0, 1, 2$):

$$a_0(\omega, t) = \frac{a_{max}}{\omega}\left[2\sin(\omega T_{1/2}) - 4\sin(\omega T_{1/2}/2)\right] \quad (26)$$

$$a_1(\omega, t) = -16a_{max}T_{1/2}\left[\frac{\cos(\omega T_{1/2})}{(\omega T_{1/2})^2}\left(1 - \frac{15}{(\omega T_{1/2})^2}\right)\right.$$
$$\left. - \frac{\sin(\omega T_{1/2})}{(\omega T_{1/2})^3}\left(6 - \frac{15}{(\omega T_{1/2})^2}\right)\right] \quad (27)$$

$$a_2(\omega, t) = -3\pi^2 a_{max}T_{1/2}\frac{\sin(\omega T_{1/2})}{(\omega T_{1/2})^3}$$
$$\times \left(1 - \frac{\pi^2}{(\omega T_{1/2})^2}\right)^{-1}\left(1 - \frac{4\pi^2}{(\omega T_{1/2})^2}\right)^{-1} \quad (28)$$

For small nObs, one expects that high frequency modes should follow adiabatically the slowly varying acceleration and return to their initial state. The values of the Fourier transform $a_i(\omega_q, t)$ then estimate how large is the *deviation* from adiabaticity. The protocol 2 shows the smallest results with $a_2(\omega_q, t) \sim 1/\omega_q^3$ because its acceleration has the smoothest (most adiabatic) onset. The difference between the temporal

profiles can be traced back to the experience of a traveller, as either an old-fashioned or a modern train takes off. As the particle increases in size, the phonon modes shift to lower frequencies and adiabatic following becomes less easier. By this mechanism, the interference contrast gets worse.

The overall contrast reduction is very tiny, however, as can be seen in Fig. 5. The symbols give the sum in Eq. (22) for one-dimensional nObs of increasing length. The overall scaling can be understood by focusing on the fundamental phonon mode, i.e., the orthogonality for $\omega_1 = \pi c/L$. We write $-\log C_{ph} = fS$ with the prefactor

$$f = \frac{(a_{max}T_{1/2})^2 k_B T_{ph}M}{\hbar^2\omega_1^2} = \left(\frac{a_{max}T_{1/2}}{\omega_1\lambda_{ph}}\right)^2 \propto L^3 \quad \text{(1D chain)} \quad (29)$$

where the phonon coherence 'length' λ_{ph} (measuring actually a displacement) turns out to be equal to the thermal de Broglie wavelength for the chain's total mass $M \sim L$, but taken at the internal temperature T_{ph}. Adopting the approximation that the fundamental tone is in the classical regime, $\hbar\omega_1 \ll k_B T_{ph}$ (at room temperature, frequencies < 6 THz or size $L > 3$ nm), the factor $f \sim T_{ph}$ makes the scaling with the phonon temperature explicit. The other factor S is a dimensionless sum over the phonon spectrum and takes the form

$$S = \sum_q \frac{\beta\omega_1^2}{2\omega_q}\coth\frac{\beta\omega_q}{2}\cos^2[(s + \tfrac{1}{2})qa]\left|\frac{a(\omega_q, t)}{a_{max}T_{1/2}}\right|^2$$
$$\simeq \frac{A_n}{(\omega_1 T_{1/2})^{2n+2}}\sum_q(\omega_1/\omega_q)^{2n+4} \propto L^{2n+2} \quad (30)$$

with $n = 0, 1, 2$. In the second line, we took $\cos^2[(s + \tfrac{1}{2})\pi a/L] \leq 1$ as upper limit and applied an upper bound for the Fourier spectra (28), leading to the numbers $A_0 = 36$, $A_1 = (16/\pi)^2$, $A_2 = 9$. For an equidistant phonon spectrum, the sum in the second line evaluates to $\zeta(2n+4) \approx 1.08232, 1.01734, 1.00408$, being dominated by its first term.

The resulting lower limit for $C_{ph} = \exp(-fS)$ is shown in Fig. 5 as dashed gray lines, while the symbols give the full sum computed numerically, showing good agreement. By placing the impurity spin near the center of the nOb, the excitation of the fundamental phonon is reduced, improving the contrast compared to Eq. (30). For the nano-diamond considered here, the temperature is such that the upper part of the phonon spectrum is in the quantum regime, $\hbar\omega_q > k_B T$, where $\coth(\beta\omega_q/2) \to 1$ stays above its classical limit. Due to the steep power laws, these modes make a negligible contribution, however, and do not exceed the estimate (30).

The main message of this plot is that the actual values for the contrast C_{ph} are extremely close to unity: the interference contrast is *not reduced at all* by the excitation of phonon modes in a linear chain. In practice, the limits will be rather set by the magnetic gradient (values given at the top of Fig. 5) and the spin coherence time (typically $\sim 200\,\mu$s).[21] The case of a fixed force (rather than acceleration) is considered in Fig. 6 below.

We have checked that a mismatch of the final velocity does not qualitatively change these results. For that, we considered models with adjusted coefficients in such a way that
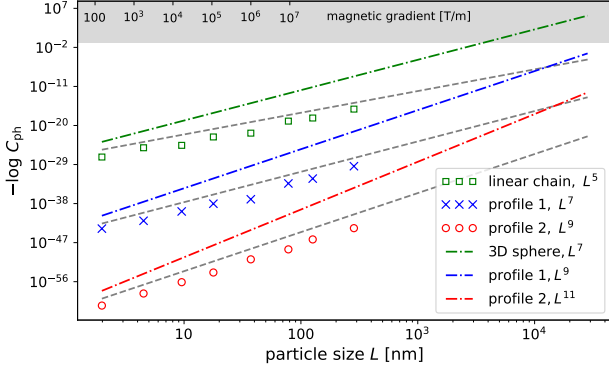
FIG. 5. Exponent in interference contrast C_{ph} for a one-dimensional chain (symbols and gray dashed) and a three-dimensional, round object (dash-dotted). log denotes the natural logarithm; in the gray-shaded area, the contrast drops below 10%. Lattice parameters for diamond at room temperature, maximum acceleration kept fixed at $a_{max} = 100\,\text{m/s}^2$, duration $2T_{1/2} = 60\,\mu\text{s}$, spin position near the center, (internal) temperature $T_{ph} = 293\,\text{K}$. The data sets marked 'linear chain' and '3D sphere' correspond to the closed-loop acceleration protocol $a_0(t)$ [Eq. (23)], while 'profile 1 and 2' correspond to Eqs. (24–25), respectively. The top scale gives the magnetic gradient required to achieve the acceleration a_{max} for a 3D object, it scales with its volume L^3.

the initial acceleration shows the same behaviour, but its integral Δv is nonzero. It turns out that for any small particle and reasonably slow gradients (in the sense given above, $c/2L > 1/T_{1/2}$), the high-frequency asymptote of the Fourier spectrum $a_1(\omega, 2T_{1/2})$ shows the same scaling, only its amplitude is changed. For our purposes, the previously discussed closed-loop case $\Delta v = 0$ is thus sufficient.

D. Three-dimensional particle

The exact calculation of phonon modes for a three-dimensional assembly of a few thousand atoms or more becomes challenging. We sketch here the modifications that are needed with respect to the linear chain. The wave vector q becomes three-dimensional, and a mode function like $u_q \cos[(n + \frac{1}{2})qa]$ becomes a vector-valued function $u_{\mathbf{q}}\mathbf{f_q}(\mathbf{r}_n)$ with mode amplitude $u_{\mathbf{q}}$. In the projection formula Eq. (6), N is now the total number of atoms in the nOb, and in Eq. (7), M becomes the total mass. The Stern-Gerlach force on the impurity spin (at $\mathbf{r}_s$) defines a direction that selects an angular pattern of emitted phonons via a scalar product with the local "polarisation vector" $\mathbf{f_q}(\mathbf{r}_s)$ of the phonon mode. The shape of the nOb and its boundary conditions determine the allowed values of q within the Brillouin zone of the crystal structure. While an exact calculation is possible (numerically) for small clusters, we focus in the following on the region near the Γ point with an approximately linear dispersion. The value $q = 0$ corresponds again to the center-of-mass mode, and we are interested in the smallest non-zero sound frequency ω_1 (think of the fundamental pitch of a musical instrument). One has to allow for different values of the speed of sound c (longi-

tudinal and transverse). In a nOb with cubic shape, the modes are separable, and we have $\omega_1 = \pi c/L$ with the linear size L. In a spherical object of diameter D, adopting a continuum model and solving the Helmholtz equation with a Neumann boundary condition, we find a dipole mode proportional to the gradient of $\cos(\theta)\left[\sin(qr)/r^2 - q\cos(qr)/r\right]$ (a spherical Bessel function) at $\omega_1 = cq$ with $q \approx 4.1632/D$. We note that experiments on resonances observed with icosahedral clusters in quasi-crystalline materials show good agreement with such a continuum analysis, even though the cluster diameters are as small as $1\,\text{nm}$.[58] A more complete analysis of the acoustic modes of a nano-sphere can be found in Ref. 29.

For a small particle (recall the typical limit $L < 30\,\text{cm}$), all phonon frequencies are way beyond the cutoff frequency $1/T_{1/2}$ of the acceleration spectrum $a(\omega_{\mathbf{q}}, 2T_{1/2})$, and the lowest phonon mode gives the dominant contribution. Its second harmonic already contributes only a few percent, depending on the protocol. This being said, we get the following rough estimate for the interference contrast for a small three-dimensional nOb:

$$-\log C_{ph} \simeq \frac{M}{2\hbar\omega_1}\coth\frac{\beta\omega_1}{2}|\mathbf{e}_z \cdot \mathbf{f}_1(\mathbf{r}_s)|^2|a(\omega_1,t)|^2$$
$$= (\cdots)\frac{Mk_B T a_{max}^2}{\hbar^2\omega_1^6 T_{1/2}^2} = (\cdots)\frac{(\Delta Z_{max})^2}{\lambda_{ph}^2}\left(\frac{L}{cT_{1/2}}\right)^6$$
$$(31)$$

where $\mathbf{e}_z$ gives the direction of the Stern-Gerlach force, and $\mathbf{f}_1(\mathbf{r}_s)$ is the fundamental phonon mode (normalized to unit maximum amplitude), evaluated at the position of the spin $\mathbf{r}_s$. In the second line, $(\cdots)$ is a numerical factor we expect to be of order unity, we adopted protocol $a_1(t)$ and assumed $\hbar\omega_1 \ll k_B T$. The scaling with the linear dimension L of the particle now gives the exponent L^9 (L^7 for $a_0(t)$ and L^{11} for $a_2(t)$), see dash-dotted lines in Fig. 5.

The second form of Eq. (31) makes contact to the seminal estimation of decoherence due to Zurek[59]: the maximum spatial splitting (at half-loop) $\Delta Z_{max} \simeq a_{max}T_{1/2}^2$ of the nOb wavepacket is compared to the phonon coherence length λ_{ph}. This huge ratio would preclude any realistic contrast, were it not compensated by the high power of the small ratio $L/cT_{1/2}$, as long as the object size L is smaller than the travelling distance of sound during the closed loop.

In Fig. 6, the contrast is shown for a different setting of parameters: here, the magnetic gradient is such that the wavepacket splits to a fixed fraction ($\sim 10\%$) of the nOb diameter. This would be a typical requirement for a Stern-Gerlach interferometer with two particles that interact via their mutual gravitational attraction, as suggested for probing quantum gravity.[5,6] We adjusted the protocol time $T_{1/2}$ to get a fixed velocity splitting Δv_{max}. In the non-shaded area of the plot, the required values are below the limits $10^6\,\text{T/m}$ and $100\,\mu\text{s}$ set by the current experimental device in the Ben-Gurion University of the Negev group. (In the shaded area, the achieved splitting is less than the targeted value.) The contrast is again excellent, and comparing to Fig. 5, these settings permit to split somewhat larger particles. The protocols a_0, a_1, and a_2 now differ by factors independent of the particle size and scale all with
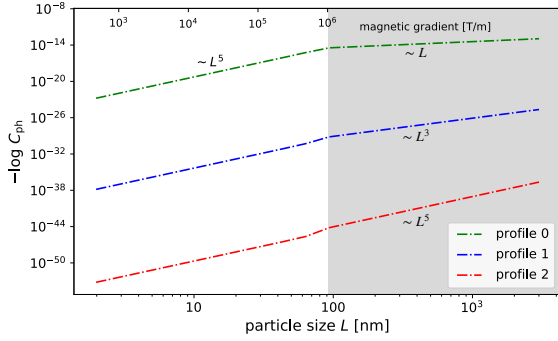
FIG. 6. Interference contrast for a three-dimensional particle. Magnetic gradient (upper scale) and duration of the loop are adjusted such that the maximum spatial splitting is a fixed fraction (10%) of the nOb size, and the maximum velocity splitting is 1 mm/s. In the gray shaded area, the required magnetic gradient and half-loop time are set to realistic maximum values (10^6 T/m and $100\,\mu$s[21]) so that the targeted splitting noted above is not achieved. Other parameters as in Fig. 5. The three data sets correspond to the closed-loop protocols of Eqs. (23–25), respectively, they show the same scaling $\sim L^5$ with the particle diameter L in the non-shaded area. The scaling laws differ in the gray area, as indicated.

the power L^5. In fact, in this setting, the ratio $L/(cT_{1/2})$ turns out to be constant ($\sim \Delta v_{\max}$ divided by the speed of sound), as long as one stays below the upper limit to $T_{1/2}$.

E. Further insight: macroscopic particle

We finally consider the limit that the acoustic modes become dense on the scale $2\pi/T_{1/2}$ of the acceleration spectrum. Although experiments will be extremely challenging (size $L > 30$ cm), we include this case as a reference.

The sum over phonon wave vectors may be replaced by an integral (recall the spacing $\Delta q = \pi/L$). Going directly to the three-dimensional case, the exponent in the contrast Eq. (22) becomes (average $|\mathbf{e}_z \cdot \mathbf{f_q}(\mathbf{r}_s)|^2 \approx \frac{1}{2}$, 3 acoustic branches)

$$-\log C_{\mathrm{ph}} \simeq \frac{3ML^3}{2\hbar} \int \frac{\mathrm{d}^3 q}{(2\pi)^3 \omega_{\mathbf{q}}} \coth \frac{\beta \omega_{\mathbf{q}}}{2} |a(\omega_{\mathbf{q}}, t)|^2$$
$$\simeq \frac{3ML^3 k_{\mathrm{B}} T}{\pi \hbar^2 c^3} \int \frac{\mathrm{d}\omega}{2\pi} |a(\omega, t)|^2 \qquad (32)$$

In the second line, we focused on the acoustic part of the dispersion relation and took the high-temperature limit. This is a good approximation, since the integration range is effectively limited by the bandwidth $2\pi/T_{1/2}$ of the acceleration spectrum. The integral gives, according to the Parseval-Plancherel formula:

$$\int \frac{\mathrm{d}\omega}{2\pi} |a(\omega, 2T_{1/2})|^2 = \int\limits_{-T_{1/2}}^{T_{1/2}} \mathrm{d}t\, a(t)^2 = C_n a_{\max}^2 T_{1/2} \qquad (33)$$

with $C_0 = 1$ for $a_0(t)$ and $C_1 = 256/315$, $C_2 = 1/2$. Note that in this regime, the three protocols are essentially equivalent.

In terms of the phonon coherence length λ_{ph}, the contrast becomes

$$-\log C_{\mathrm{ph}} \simeq (\cdots)\left(\frac{\Delta Z_{\max}}{\lambda_{\mathrm{ph}}}\right)^2 \left(\frac{L}{cT_{1/2}}\right)^3 \qquad (34)$$

where again $\Delta Z_{\max} \simeq a_{\max} T_{1/2}^2$ and $(\cdots)$ is a numerical coefficient of order one. Since now the last factor is larger than unity (large particle), coherent splitting can only occur over distances smaller than $\lambda_{\mathrm{ph}} \ll 10^{-15}$ m. For the mass region stated in the beginning of this section, non-negligible splitting will thus be impossible.

It is interesting to note that when the acceleration is expressed by the maximum force, $F_{\max} = M a_{\max}$, the object mass M drops out of this estimate. In terms of magnetic gradient and protocol time, the requirement $C_{\mathrm{ph}} \geq 10\%$ gives the inequality

$$\frac{T_{1/2}}{\mu\mathrm{s}} \left(\frac{b_{\max}}{\mathrm{T/m}}\right)^2 \leq (\cdots) 10^{15} \frac{[\rho/(\mathrm{g/cm}^3)][c/(10^3\,\mathrm{m/s})]^3}{(\mu/\mu_B)^2 (T_{\mathrm{ph}}/300\,\mathrm{K})} \qquad (35)$$

This upper limit is larger than the parameters available in current experiments, but only by a few orders of magnitude. The main challenge seems to be that the corresponding forces on large objects are too small to split a wavepacket by a significant fraction of the object size (see Fig. 6).

IV. DISCUSSION AND CONCLUSION

In this work we examined the coherent splitting of a nano-object with an embedded single spin, in a full-loop Stern-Gerlach interferometer. We addressed the question of whether the internal degrees of freedom (phonons) pose a problem, as they are excited by kicks in opposite directions for the two wavepackets. This may cause distinguishability to the point of orthogonality.

We looked at 1D and 3D models, assuming phonon normal modes in the harmonic approximation, and examined the scaling of the contrast reduction with the particle size at fixed acceleration or fixed maximal separation. We looked at the coherence drop solely due to phonons, assuming that the closing (overlap) of other degrees of freedom (position, momentum, rotation) is perfect. We took care to make use of realistic experimental numbers for the magnetic gradients and spin coherence time inside a nano-object.

As expected, we find that achieving complete overlap of the phonon state is impossible. However, the suppression of coherence for practical numbers is found to be minimal. We examined several temporal profiles of the magnetic field and found that the smoother the profile (namely, slower onset of the magnetic field), the higher the eventual coherence. This is caused by an increasingly adiabatic behavior of the phonon modes. We also find that a non-zero temperature does not significantly alter the contrast. However, we find that once we go for higher masses, phonons indeed suppress the possibility of coherent interferometry, and this may indeed turn out to be a fundamental limit for creating massive superpositions in the future.

The final conclusion is therefore that phonon dynamics are not an inhibiting factor for a large range of parameters in nano-object Stern-Gerlach interferometry, making this method highly relevant for the fundamental experiments noted in the Introduction.

[1] M. P. Bronstein, "Quantentheorie schwacher Gravitationsfelder (Quantization of gravitational waves)," Phys. Zeitschr. Sowjetunion **9**, 140–57 (1936), reprinted in Gen. Relativ. Gravit. **44**, 267–83 (2012).

[2] W. Marshall, C. Simon, R. Penrose, and D. Bouwmeester, "Towards quantum superpositions of a mirror," Phys. Rev. Lett. **91**, 130401 (2003).

[3] R. Marshman, A. Mazumdar, G. Morley, P. Barker, S. Hoekstra, and S. Bose, "Mesoscopic interference for metric and curvature, and gravitational wave detection," New J. Phys. **22**, 083012 (2020).

[4] C. Wan, M. Scala, G. Morley, A. Rahman, H. Ulbricht, J. Bateman, P. Barker, S. Bose, and M. Kim, "Free nano-object Ramsey interferometry for large quantum superpositions," Phys. Rev. Lett. **117**, 143003 (2016).

[5] C. Marletto and V. Vedral, "Gravitationally induced entanglement between two massive particles is sufficient evidence of quantum effects in gravity," Phys. Rev. Lett. **119**, 240402 (2017).

[6] S. Bose, A. Mazumdar, G. Morley, H. Ulbricht, M. Toroš, M. Paternostro, A. Geraci, P. Barker, M. Kim, and G. Milburn, "Spin entanglement witness for quantum gravity," Phys. Rev. Lett. **119**, 240401 (2017).

[7] R. Marshman, A. Mazumdar, and S. Bose, "Locality and entanglement in table-top testing of the quantum nature of linearized gravity," Phys. Rev. A **101**, 052110 (2020).

[8] C. Marletto and V. Vedral, "On the testability of the equivalence principle as a gauge principle detecting the gravitational t^3 phase," Front. Phys. **8**, 176 (2020).

[9] D. Carney, H. Müller, and J. Taylor, "Using an atom interferometer to infer gravitational entanglement generation," Phys. Rev. X Quantum **2**, 030330 (2021), erratum: PRX Quantum 3, 010902 (2022).

[10] D. Carney, H. Müller, and J. Taylor, "Quantum superposition of massive objects and collapse models," Phys. Rev. A **84**, 052121 (2011).

[11] G. Gasbarri, A. Belenchia, M. Carlesso, S. Donadi, A. Bassi, R. Kaltenbaek, M. Paternostro, and H. Ulbricht, "Testing the foundation of quantum physics in space via interferometric and non-interferometric experiments with mesoscopic nanoparticles," Commun. Phys. **4**, 155 (2021)

[12] M. Rademacher, J. Millen, and Y. L. Li, "Quantum sensing with nanoparticles for gravimetry: when bigger is better," Adv. Opt. Techn. **9**, 227 (2020).

[13] A. Rahman, A. Frangeskou, M. Kim, S. Bose, G. Morley, and P. Barker, "Burning and graphitization of optically levitated nanodiamonds in vacuum," Sci. Rep. **6**, 21633 (2016).

[14] A. Albrecht, A. Retzker, and M. B. Plenio, "Testing quantum gravity by nanodiamond interferometry with nitrogen-vacancy centers," Phys. Rev. A **90**, 033834 (2014)

[15] Y. Fein, P. Geyer, P. Zwick, F. Kiałka, S. Pedalino, M. Mayor, S. Gerlich, and M. Arndt, "Quantum superposition of molecules beyond 25 kDa," Nature Phys. **15**, 1242 (2019).

[16] A. Shayeghi, P. Rieser, G. Richter, U. Sezer, J. H. Rodewald, P. Geyer, T. J. Martinez, and M. Arndt, "Matter-wave interference of a native polypeptide," Nature Commun. **11**, 1447 (2020).

[17] H. Pino, J. Prat-Camps, K. Sinha, B. P. Venkatesh, and O. Romero-Isart, "On-chip quantum interference of a superconducting microsphere," Quantum Sci. Technol. **3**, 25001 (2018).

[18] H. Pino, J. Prat-Camps, K. Sinha, B. Venkatesh, and O. Romero-Isart, "Coherent inflation for large quantum superpositions of microspheres," New J. Phys. **19**, 719711 (2017).

[19] Y. Margalit, O. Dobkowski, Z. Zhou, O. Amit, Y. Japha, S. Moukouri, D. Rohrlich, A. Mazumdar, S. Bose, C. Henkel, and R. Folman, "Realization of a complete Stern–Gerlach interferometer: Towards a test of quantum gravity," Science Adv. **7**, eabg2879 (2021).

[20] Y. Japha and R. Folman, "Role of rotations in Stern-Gerlach interferometry with massive objects," preprint quant-ph arXiv:2202.10535 (2022).

[21] M. E. Trusheim, L. Li, A. Laraoui, E. H. Chen, H. Bakhru, T. Schröder, O. Gaathon, C. A. Meriles, and D. Englund, "Scalable fabrication of high purity diamond nanocrystals with long-spin-coherence nitrogen vacancy centers," Nano Lett. **14**, 32–36 (2013) .

[22] J. Bateman, S. Nimmrichter, K. Hornberger, and H. Ulbricht, "Near-field interferometry of a free-falling nanoparticle from a point-like source," Nature Commun. **5**, 5788 (2014) .

[23] D. E. Chang, C. A. Regal, S. B. Papp, D. J. Wilson, J. Ye, O. Painter, H. J. Kimble, and P. Zoller, "Cavity opto-mechanics using an optically levitated nanosphere," Proc. Natl. Acad. Sci. (U.S.A.) **107**, 1005 (2010) .

[24] T. W. van de Kamp, R. J. Marshman, S. Bose, and A. Mazumdar, "Quantum gravity witness via entanglement of masses: Casimir screening," Phys. Rev. A **102**, 062807 (2020) .

[25] M. Schut, J. Tilly, R. J. Marshman, S. Bose, and A. Mazumdar, "Improving resilience of quantum-gravity-induced entanglement of masses to decoherence using three superpositions," Phys. Rev. A **105**, 032411 (2022) .

[26] P. Sonnentag and F. Hasselbach, "Measurement of decoherence of electron waves and visualization of the quantum-classical transition," Phys. Rev. Lett. **98**, 200402 (2007).

[27] A. Xuereb, H. Ulbricht, and M. Paternostro, "Optomechanical interface for probing matter-wave coherence," Sci. Rep. **3**, 3378 (2013).

[28] D. Hümmer, R. Lampert, K. Kustura, P. Maurer, C. Gonzalez-Ballestero, and O. Romero-Isart, "Acoustic and optical properties of a fast-spinning dielectric nanoparticle," Phys. Rev. B **101**, 205416 (2020).

[29] C. Gonzalez-Ballestero, D. Hümmer, J. Gieseler, and O. Romero-Isart, "Theory of quantum acoustomagnonics and acoustomechanics with a micromagnet," Phys. Rev. B **101**, 125404 (2020).

[30] C. Gonzalez-Ballestero, J. Gieseler, and O. Romero-Isart, "Quantum acoustomechanics with a micromagnet," Phys. Rev. Lett. **124**, 093602 (2020).

[31] M. Strungaru, M. O. A. Ellis, S. Ruta, O. Chubykalo-Fesenko, R. F. L. Evans, and R. W. Chantrell, "Spin-lattice dynamics model with angular momentum transfer for canonical and microcanonical ensembles," Phys. Rev. B **103**, 024429 (2021) .

[32] J. S. Pedernales, G. W. Morley, and M. B. Plenio, "Motional dynamical decoupling for interferometry with macroscopic particles," Phys. Rev. Lett. **125**, 023602 (2020) .

[33] R. J. Marshman, A. Mazumdar, R. Folman, and S. Bose, "Constructing large quantum superpositions," Phys. Rev. Research, in press (2022), arXiv:2105.01094.

[34] We checked that in the limit $q \to 0$, one recovers the center-of-mass dynamics of Eq. (4).

[35] H. J. Lipkin, "Debye-Waller Factor in Mössbauer interference experiments," Phys. Rev. **123**, 62–63 (1961).

[36] A. C. Levi and H. Suhl, "Quantum theory of atom–surface scattering: Debye–Waller factor," Surf. Sci. **88**, 221–54 (1979).

[37] O. Sild and K. Haller, eds., *Zero-Phonon Lines and Spectral Hole Burning in Spectroscopy and Photochemistry* (Springer, 1988).

[38] D. Hsu and J. L. Skinner, "On the thermal broadening of zero-phonon impurity lines in absorption and fluorescence spectra," J. Chem. Phys. **81**, 1604–13 (1984).

[39] W. P. Schleich, *Quantum Optics in Phase Space* (Wiley-VCH, Berlin, 2001).

[40] W. Vogel, D.-G. Welsch, and S. Wallentowitz, *Quantum Optics – An Introduction* (Wiley-VCH, Berlin Weinheim, 2001).

[41] P. W. Milonni, *The Quantum Vacuum* (Academic Press Inc., San Diego, 1994).

[42] O. M. Friesch, I. Marzoli, and W. P. Schleich, "Quantum carpets woven by Wigner functions," New J. Phys. **2**, 4–4 (2000).

[43] K. Bongs, R. Launay, and M. Kasevich, "High-order inertial phase shifts for time-domain atom interferometers," Appl. Phys. B **84**, 599–602 (2006).

[44]O. Amit, *Matter-Wave Interferometry on an Atom Chip*, Ph.D. thesis, Ben-Gurion University of the Negev, Beer Sheva (2020).

[45]U. Delić, M. Reisenbauer, K. Dare, D. Grass, V. Vuletić, N. Kiesel, and M. Aspelmeyer, "Cooling of a levitated nanoparticle to the motional quantum ground state," Science **367**, 892–95 (2020).

[46]F. Tebbenjohanns, M. Frimmer, V. Jain, D. Windey, and L. Novotny, "Motional sideband asymmetry of a nanoparticle optically levitated in free space," Phys. Rev. Lett. **124**, 013603 (2020).

[47]F. Tebbenjohanns, M. L. Mattana, M. Rossi, M. Frimmer, and L. Novotny, "Quantum control of a nanoparticle optically levitated in cryogenic free space," Nature **595**, 378–82 (2021).

[48]L. Magrini, P. Rosenzweig, C. Bach, A. Deutschmann-Olek, S. G. Hofer, S. Hong, N. Kiesel, A. Kugi, and M. Aspelmeyer, "Real-time optimal quantum control of mechanical motion at room temperature," Nature **595**, 373–77 (2021).

[49]E. Wigner, "On the quantum correction for thermodynamic equilibrium," Phys. Rev. **40**, 749–59 (1932).

[50]N. G. van Kampen, "A soluble model for quantum mechanical dissipation," J. Stat. Phys. **78**, 299–310 (1995).

[51]G. M. Palma, K.-A. Suominen, and A. K. Ekert, "Quantum computers and dissipation," Proc. Roy. Soc. (London) A **452**, 567–84 (1996).

[52]Y. Romach, C. Müller, T. Unden, L. J. Rogers, T. Isoda, K. M. Itoh, M. Markham, A. Stacey, J. Meijer, S. Pezzagna, B. Naydenov, L. P. McGuinness, N. Bar-Gill, and F. Jelezko, "Spectroscopy of surface-induced noise using shallow spins in diamond," Phys. Rev. Lett. **114**, 017601 (2015).

[53]E. D. Herbschleb, H. Kato, Y. Maruyama, T. Danjo, T. Makino, S. Yamasaki, I. Ohki, K. Hayashi, H. Morishita, M. Fujiwara, and N. Mizuochi, "Ultra-long coherence times amongst room-temperature solid-state spins," Nature Commun. **10**, 3766 (2019).

[54]N. Bar-Gill, L. Pham, A. Jarmola, D. Budker, and R. Walsworth, "Solid-state electronic spin coherence time approaching one second," Nature Commun. **4**, 1743 (2013).

[55]A. Waxman, H. Schlussel, D. Groswasser, V. M. Acosta, L.-S. Bouchard, D. Budker, and R. Folman, "Diamond magnetometry of superconducting thin films," Phys. Rev. B **89**, 054509 (2014).

[56]Y. Schlussel, T. Lenz, D. Rohner, Y. Bar-Haim, L. Bougas, D. Groswasser, M. Kieschnick, E. Rozenberg, L. Thiel, A. Waxman, J. Meijer, P. Maletinsky, D. Budker, and R. Folman, "Wide-field imaging of superconductor vortices with electron spins in diamond," Phys. Rev. Applied **10**, 034032 (2018).

[57]Y. Rosenzweig, Y. Schlussel, and R. Folman, "Probing the origins of inhomogeneous broadening in nitrogen-vacancy centers with Doppler-free-type spectroscopy," Phys. Rev. B **98**, 014112 (2018).

[58]E. Duval, L. Saviot, A. Mermet, and D. B. Murray, "Continuum elastic sphere vibrations as a model for low lying optical modes in icosahedral quasicrystals," J. Phys.: Condens. Matter **17**, 3559–65 (2005).

[59]W. H. Zurek, "Decoherence and the transition from quantum to classical – revisited," (2003), earlier version published in *Physics Today* **44**, 36-44 (Oct 1991), preprint quant-ph/0306072.